3D-Multi-Echo Radial Imaging of ^{23}Na (3D-MERINA) for time-efficient multi-parameter tissue compartment mapping

Running title:

3D-Multi-Echo Radial Imaging of ^{23}Na (3D-MERINA)

Yasmin Blunck[1,3]*, Sonal Josan[2], Syeda Warda Taqdees[1,3], Brad A. Moffat[3], Roger J. Ordidge[3], Jon O. Cleary[3†], Leigh A. Johnston[1,3†]

[1] *Biomedical Engineering, University of Melbourne, Parkville, Australia*

[2] *Siemens Healthcare, Melbourne, Australia*

[3] *Melbourne Brain Centre Imaging Unit, Anatomy and Neuroscience, University of Melbourne, Parkville, Australia*

[†] *joint senior authors*

*correspondence: Melbourne Brain Centre Imaging Unit, Kenneth Myer Building, University of Melbourne, 30 Royal Parade, Parkville VIC 3052, Australia

email: blunck.yasmin@gmail.com

Key words: Sodium (^{23}Na) MRI; bi-exponential decay; transverse relaxation; tissue compartment mapping;

Word count: 5135

Abstract

Purpose: This work demonstrates a 3D radial multi-echo acquisition scheme for time-efficient ^{23}Na MR-signal acquisition and analysis. Echo reconstructions were used to produce SNR-enhanced ^{23}Na-images and parameter maps of the bi-exponential T2* decay.

Methods: A custom-built sequence for radial multi-echo acquisition was proposed for acquisition of a series of 3D volumetric ^{23}Na-images. Measurements acquired in a phantom and in vivo human brains were analyzed for SNR enhancement and multi-component T2* estimation.

Results: Rapid gradient re-focused imaging acquired 38 echoes within a TR of 160 ms. Signal-averaging of multi-TE measurements showed an average brain tissue SNR enhancement of 34% compared to single-TE images across subjects. Phantom and in vivo measurements detected distinguishable signal decay characteristics for fluid and solid media. Mapping results were investigated in phantom and in vivo experiments for sequence timing optimization and signal decay analysis. The T2* mapping results were consistent with previously reported values, and facilitated fluid-signal discrimination.

Conclusion: The proposed method offers an efficient ^{23}Na-imaging scheme that extends existing ^{23}Na-MRI sequences by acquiring signal decay information with no increase in time or SAR. The resultant SNR-enhanced ^{23}Na-images and estimated T2* signal decay characteristics offer great potential for detailed investigation of tissue compartment characterization and clinical application.

Key words: Sodium (^{23}Na) MRI; bi-exponential decay; transverse relaxation; tissue compartment mapping;

Introduction

^{23}Na is the second most abundant MR-observable nucleus in biological tissue and plays a vital role in cell physiology. The electrochemical gradient between intra- and extracellular ^{23}Na concentration is a crucial component of a cell's physiology and is strongly dependent on the cell's metabolism and its membrane integrity. Hence, disturbances of this delicate mechanism are considered as a sensitive, early indicator for cell breakdown and provide an insight into cell integrity and tissue viability (1-3). Based on its involvement in energy as well as structural processes, ^{23}Na is a potential tool for the detection of metabolic parameters; its capabilities as a biomarker aimed at extending clinical MRI to earlier diagnosis and therapy response measurements have been discussed, as well as the application to the detection of diseases without anatomic abnormalities (3). Early studies of ^{23}Na-MRI date back to the 1980s (4,5) and with advancements in hardware and acquisition strategies (6-9), several more recent studies have investigated the potential of ^{23}Na-MRI across a variety of diseases ranging from neurodegenerative diseases (10,11), stroke (12,13) and tumors (14-16) to musculoskeletal pathologies (17-20), and others (21,22).

MR experiments on ^{23}Na nuclei detect signal originating from complex electrical and dynamic spin interactions. Other than ^{1}H nuclei, electric charges of ^{23}Na nuclei are non-spherically distributed causing an electric quadrupolar moment based on the interaction between the ^{23}Na nucleus and its environment. Consequently, ^{23}Na nuclei are not just affected by local magnetic field interactions but also exhibit impact from local electric fields. ^{23}Na nuclei have a spin of 3/2 and four corresponding discrete energy states (3/2, 1/2, -1/2, -3/2). Single-quantum coherence measurements (i.e. acquisitions under single 90° RF-pulses without enhanced filtering techniques) detect transitions between adjacent energy levels. In an isotropic system, e.g fluid media, the effects of magnetic and electric fields average out resulting in identical transition rates for all single quantum coherences and, hence, display mono-exponential decay behaviour. In macroscopically structured environments, nuclei experience non-vanishing average electric field gradients leading to a shift in energy levels that produces a frequency splitting on the spectrum (23,24). These interactions cause the satellite transitions (i.e. -3/2 -> -1/2 and 1/2 -> 3/2) to occur at

faster rates than the central transitions (-1/2 -> 1/2) and result in bi-exponential T2 decay. Both ^{23}Na-signal T2 decay components in anisotropic systems exhibit faster relaxation than the mono-exponential relaxation in isotropic environments (24-26). The complex interactions that give rise to the ^{23}Na signal suggest the potential for inference of underlying macroscopic structure (27).

Sensitizing ^{23}Na contrast to reveal information about structure has been an active field of research, focusing predominantly on the selective detection of intracellular ^{23}Na contents. Several approaches have been suggested for intracellular ^{23}Na weighted acquisitions: chemical shift reagents for a selective frequency offset of extracellular ^{23}Na signal (28,29), triple-quantum-filtered (TQF) imaging facilitating the selective detection of higher quantum coherences (30-35), fluid-suppression based on inversion recovery for an attenuation of fluid ^{23}Na signal (36-41). Recent work by Qian et al. (42) suggested the use of ^{23}Na-signal decay for the inference of structural components. The inference of metabolic and macrostructural information in healthy and pathological processes is promising for clinical MRI studies.

Despite recent advancements in hardware, the number of ^{23}Na-MRI based clinical studies is still comparatively small (22). The main challenges for the advancement of ^{23}Na-MRI are low SNR coupled with relatively high SAR exposure (particularly at high fields) and correspondingly prolonged scan times. Recent studies have addressed these challenges by more efficient acquisition methods: SISTINA (43) allows for the detection of single and triple-quantum filtered images in a single TQF-acquisition. Benkhedah et al. (44) proposed gradient-selected and phase-cycling difference imaging approaches for the acquisition of ^{23}Na-density and single quantum filtered images with the potential for inferring triple-quantum filtered image contrasts.

Our primary contribution is a new acquisition approach based on 3D Multi-Echo Radial Imaging in ^{23}NA (3D-MERINA), from which multiple parameter maps can be inferred from a single scan. The relatively long acquisition times typical of ^{23}Na-MRI originate from SAR limitations and the need for full longitudinal signal recovery in ^{23}Na-density weighted

acquisitions. Our method fills vacant imaging time with the acquisition of additional gradient re-focused echoes. We demonstrate that through the use of radial imaging, echoes can be acquired rapidly and subsequently exploited for SNR enhancement and the estimation of T2* parameter maps, while still providing ^{23}Na-density weighted images for quantification purposes.

Methods

Sequence Design - 3D Multi-Echo Radial Imaging of 23Na (3D-MERINA)

Imaging was performed on a research 7T MRI scanner (Siemens Healthcare, Erlangen, Germany) with a transmit/receive dual-tuned ^{1}H-^{23}Na head coil (QED, Mayfield Village, Ohio USA). The ^{23}Na-based imaging sequence consisted of a non-selective hard pulse (duration 500 μs) with a custom-built 3D radial acquisition scheme. The placement of readout spokes was based on Saff and Kuijlaars' algorithm (45) for homogeneous projection distribution. For a total number of projections N, the spherical coordinates of each projection, $\theta \in [0,\pi]$ and $\phi \in [0,2\pi]$ were determined via:

$$\theta_k = \arccos(h_k), \quad h_k = -1 + \frac{2(k-1)}{N-1}, \quad 1 \le k \le N$$
$$\phi_k = \left(\phi_{k-1} + \frac{3.6}{\sqrt{N}} \frac{1}{\sqrt{1-{h_k}^2}}\right) mod\ 2\pi, \quad 2 \le k \le N-1, \quad \phi_1 = \phi_N = 0 \qquad [1]$$

The 3D-MERINA sequence acquires multiple gradient echoes via repetitive gradient re-focusing along each projection angle. The first echo is based on a center-out half-projection, while consecutive echoes are acquired as full-projections (Figure 1). The number of acquired echoes depends on the readout duration, T_{RO}, and repetition time, TR.

T_{RO} optimization

The choice of sampling durations (T_{RO}) in radial imaging implies a well-known optimization problem between achievable SNR and T2*-induced blurring (46). For a given resolution and FOV, shorter T_{RO} requires stronger gradients and, hence, gives rise to a higher bandwidth. Given the direct proportionality between BW and thermal noise in the acquired signal, T_{RO} influences the final image quality, i.e. longer T_{RO} enhance SNR. However, due to concomitant T2* signal decay, the choice of T_{RO} introduces a trade-off

between resultant SNR and PSF (7,46). The bi-exponential decay characteristics and broad range of ^{23}Na transverse relaxation times in biological tissue complicate the determination of an optimal T_{RO}. Based on reported relations between short and long decay times of $T2^*_{long}/T2^*_{short} \approx 10$, it was found that $T_{RO} = 0.14\ T2^*_{long}$ yielded optimal image results in 3D radial projection imaging (7) which consequently suggests a T_{RO} between 2.1 and 4.2 ms for commonly reported brain tissue $T2^*_{long}$ components of 15-30ms (1).

For the characterization of fast bi-exponential signal decay the 3D-MERINA acquisition scheme expands the constraints of good SNR and narrow PSF to include the extra requirement of multiple fast echo detections. The additional optimization constraint was investigated experimentally for an isotropic resolution of 3.1 mm and a FOV of 20 cm. Phantom measurements were analyzed with regards to the number of measurable echoes with good signal to noise characteristics. The duration and number of echoes with sufficient signal quality, i.e. $y_{TE} \geq 2\ \mu_{noise}$, were used to determine an optimal T_{RO} for low ^{23}Na concentrations in fast decaying solid environments.

Reconstruction

Images were reconstructed offline via Kaiser-Bessel re-gridding onto an isotropic, 3.1 mm resolution grid in Matlab. The re-gridding oversampling factor was set to 1.5. Prior to re-gridding, raw projection data was weighted to compensate for density inhomogeneities by an approach described by Nielles-Vallespin et al.(47)

$$w_s = \frac{\pi}{N}\left[\left(\frac{k_{s+1}}{2}\right)^2 + \left(\frac{k_s}{2}\right)^2\right] \qquad s = 0, \dots, S-1 \qquad [2]$$

where N is the number of half-projections acquired, and S the number of sampling points along each spoke. It should be noted that weighting on re-focused echoes is halved compared to the initial echo based on the acquisition of full-projections. A Hann-filter was applied to raw projection data for the reduction of Gibbs ringing artifacts.

SNR enhancement

The combination of multiple echoes for SNR enhancement was investigated via averaging of raw k-space data prior to re-gridding. The SNR was determined according to Gudbjartsson and Patz (48).

Experiments

Phantom

Initial experiments were performed on a phantom to investigate optimal timing parameters. Phantom acquisitions were furthermore utilized to assess the sequence's capability of measuring bi-exponential decay behavior across different media and ^{23}Na concentrations. The phantom consisted of 16 packed vials surrounded by air. Each had a diameter of 3 cm and contained a combination of saline concentration (30, 70, 110 and 150 mM) and agar level (liquid, 1% 3% and 6%). ^{23}Na-MRI was performed with 3D-MERINA as described above. TR was set to 160 ms to allow for a complete signal recovery between 90° RF-excitations. To assess the image quality across a number of readout durations, measurements with T_{RO} ranging from 1 to 6 ms were acquired. The initial TE was kept constant at 400 µs, and was defined as the time interval between the center of the pulse and the gradient and ADC onset. The following TEs as well as the number of measurable echoes depended on T_{RO}. The shortest chosen T_{RO} (1 ms) permitted the detection of 75 echoes; for the longest T_{RO} experiment (6 ms) 11 echoes were recorded. The acquired FOV was 20 cm. N=10,000 projections were sampled, leading to an acquisition time of 26min 40s. B0-field shimming was based on a vendor-provided 3D shimming routine and was performed on the ^{1}H channel. Shim optimization was repeated 10 times prior to each acquisition.

In vivo

All human imaging was conducted with the approval of the University of Melbourne Human Research Ethics Committee and volunteers gave an informed consent prior to the experiment. Human in vivo acquisitions are performed on four healthy volunteers (2 male, 2 female). ^{23}Na-MRI was based on 3D-MERINA acquisitions as described in the phantom experiment. T_{RO} was kept at an optimized value of 2 ms allowing for the detection of 38 echoes while maintaining good SNR properties. The shimming procedure and other

imaging parameters were identical to the phantom measurement above. For further analysis of image characteristics, additional ^{1}H-based images were acquired: A ^{1}H-FLASH image was measured with TR = 11 ms, TE = 3.06 ms, 14° flip angle, 1 mm isotropic resolution, acquisition time 6min 12sec. Brain tissue segmentation was based on a ^{1}H-MP2RAGE image acquired at inversion times 700 and 2700 ms with 5° and 6° flip angle, TR = 4900 ms, TE = 2.94 ms, GRAPPA-factor 4, 0.9 mm isotropic resolution, acquisition time 6min. ^{1}H-MP2RAGE were imaged using a 32-channel head-coil (Nova Medical Inc., Wilmington MA, USA) in a separate imaging sessions.

Additional analysis of estimated parameter maps in human in vivo data was performed on tissue segmentations taken from the ^{1}H-weighted acquisitions. The processing pipeline was done in FSL (49) and involved 3 main steps: 1) Brain extraction on the FLASH image, 2) registration of brain mask onto MP2RAGE image and tissue segmentation (CSF, Gray Matter, White Matter) of masked MP2RAGE, and 3) registration of segmented brain regions via the FLASH image onto the ^{23}Na-image. The interpolation of segmented brain regions onto the coarser ^{23}Na-image resolution results in masks with strong partial volume effects. A threshold of 2/3 was applied to each mask to limit the contamination of partial volume effects in the analysis.

T2* decay parameter mapping

Signal model

Spin 3/2 nuclei entail 4 quantum states that are shaped by dipolar and quadrupolar interactions. The latter is caused by non-spherical electrical environments around the nucleus and results in symmetric perturbations of the satellite Zeeman energy levels. The effects are observable as a bi-exponential transverse relaxation process. It has been shown that the satellite and central transitions contribute to 60% and 40% of the total ^{23}Na signal and represent short and long T2* decay, respectively (24).

The applied signal model was, therefore, defined as a bi-exponential decay function with fixed component ratios given by

$$A^{bi}(t, \boldsymbol{\beta_{bi}}) = A_0 \left[0.6 \exp\left(-\frac{t}{T2^*_{short}}\right) + 0.4 \exp\left(-\frac{t}{T2^*_{long}}\right)\right], \boldsymbol{\beta_{bi}} = \left[T2^*_{short}, T2^*_{long}, A_0\right]^T \quad [3]$$

where A is the signal, $T2^*_{short}$ and $T2^*_{long}$ are the short and long decay parameters (ms), respectively, and A_0 the initial maximum signal.

The decay parameters are affected by the correlation time (t_c), i.e. the average time it takes a particle to rotate by one radian. If t_c is short, i.e. $t_c \leq (2\omega_0)^{-1}$, the effects of electric field gradients average to zero. This results in a single resonance line in the spectrum, i.e. slow and fast relaxation times coincide. The correlation time, t_c, reflects the interaction with macromolecular charges (50) and is therefore short in liquid environments. In human brain ^{23}Na-imaging, short t_c are expected to occur in CSF areas and its signal decay is therefore appropriately described by a mono-exponential decay model

$$A^{mono}(t, \boldsymbol{\beta_{mono}}) = A_0 \exp\left(-\frac{t}{T2^*_{long}}\right), \qquad \boldsymbol{\beta_{mono}} = \left[T2^*_{long}, A_0\right]^T . \qquad [4]$$

To account for the complex decay characteristics of both brain tissue and CSF, the parameter estimation process was performed in two steps. Initially, all voxels were fit by a bi-exponential signal model (Eq 3), using a Rician noise model and a maximum likelihood estimation approach. The $T2^*_{short}$ estimate was then checked for plausibility: very short (<0.3 ms) and long (>7 ms) $T2^*_{short}$ were classified as liquid environments and consequently re-fit by the mono-exponential decay model (Eq 4).

The lower plausibility threshold was determined by the measurement setup as the initial echo at TE_0 = 400 µs does not practically enable the detection of shorter decay times. The upper threshold was taken from literature commonly reporting biological tissue $T2_{short}$ values around 0.5 to 3 ms (4,51) however, also values up to 6 ms have been observed (27). Compared to biological tissues, relaxation times of ^{23}Na signal in agar media have been found to show longer $T2^*_{short}$ components (25,52) – 4.2 ms and 2.7 ms $T2_{short}$ decays have been reported in 8.9% and 10% agar, respectively. Higher concentrations of agar lead to longer t_c and, hence, cause shorter T2 decays. Due to the lower agar level in our phantom study, therefore, slightly longer $T2^*_{short}$ components are expected. Consequently, the upper plausibility threshold for $T2^*_{short}$ was set to 13 ms (3-4 times the reported value) in phantom parameter estimation.

Parameter Estimation

The estimation of decay parameters was performed on magnitude images, the noise characteristics of which are well-known to be Rician distributed (48). It is particularly important to model the Rician noise, given the low SNR regime under which ^{23}Na imaging occurs.

The Rician probability density function is

$$p_{Rician}(y|A,\sigma) = \frac{y}{\sigma^2}\exp[-(y^2+A^2)]\,/2\sigma^2\;\; I_0\left(\frac{A\,y}{\sigma^2}\right) \quad [5]$$

where I_0 is the 0th-order Bessel function of the first kind, y is the measured data (from a single voxel) and A is the noise-free signal model. The parameter, σ, is the standard deviation of the Gaussian noise in the underlying complex image data.

In zero-signal (noise) regions, i.e. $A \rightarrow 0$, the Rician pdf simplifies to a Rayleigh distribution

$$p_{Rayleigh}(y|\sigma) = \frac{y}{\sigma^2}\,\exp -(y^2/2\sigma^2) \quad [6]$$

The Rayleigh mean is $\mu = \sigma\sqrt{(\pi/2)}$, and is used to estimate σ. It should be noted that half vs. full-projection data collection affects the noise characteristics, leading to a higher noise variance σ^2 in TE_0 compared to the following TE data points. In the estimation process σ^2 was consequently defined for every TE reconstruction individually.

Let $\boldsymbol{\beta}$ be the parameter vector of a decay model (bi- or mono-exponential). The MLE approach estimates decay parameters via maximizing the likelihood,

$$L(\boldsymbol{\beta}|\boldsymbol{y},\boldsymbol{\sigma}) = \prod_{i=1}^{m} p_{Rician}(y_i|A(TE_i,\boldsymbol{\beta}),\sigma_i). \quad [7]$$

Here m is the number of echo measurements and y_i, TE_i and σ_i the i^{th} measured signal, echo time, and noise variance, respectively. The function $A(.)$ is the bi-exponential or mono-exponential signal model (Eq 3 and 4), with respective parameter vectors $\boldsymbol{\beta}$. It is computationally more efficient to optimize the log-likelihood function,

$$\log L = \sum_{i=1}^{m} log\left(\frac{y_i}{{\sigma_i}^2}\right) - \sum_{i=1}^{m}\frac{y_i^2 + A(TE_i,\boldsymbol{\beta})^2}{2{\sigma_i}^2} + \sum_{i=1}^{m}\log I_0\left(\frac{A(TE_i,\boldsymbol{\beta})\;\; y_i}{{\sigma_i}^2}\right) \quad [8]$$

with respect to $\boldsymbol{\beta}$

$$\hat{\boldsymbol{\beta}} = \arg\max_{\boldsymbol{\beta}} \log L. \quad [9]$$

The Maximum-Likelihood parameter estimation was implemented in Matlab using a constrained nonlinear multivariable solver. Initial conditions for in-vivo estimations were based on previously reported values (1) and set to 1.5 ms for $T2^*_{short}$ and 20 ms for $T2^*_{long}$. Previous studies of bi-exponential ^{23}Na decay in 8.9% and 10% agar observed $T2_{short}$ values of 4.2 ms and 2.7 ms and $T2_{long}$ decay of 18 ms and 14.8 ms, respectively (25,52). Due to lower agar level in this study, slightly longer $T2^*_{short}$ components are expected and the estimation process for phantom data was, hence, initialised at 6 ms and 20 ms for $T2^*_{short}$ and $T2^*_{long}$, respectively.

Results

3D-MERINA readout duration optimization

The effect of T_{RO} on multi-echo acquisition was evaluated experimentally. Phantom experiments for T_{RO} ranging from 1-5 ms were performed to identify optimal timing parameters allowing for rapid multi-echo acquisition while maintaining good SNR characteristics for a subsequent decay analysis.

Figure 2a shows normalized signal decays in the central voxel of the 30 mM phantom vials (liquid and 6% agar) for each T_{RO} acquisition. An illustration of signal decays across all saline concentrations and agar level for each T_{RO} can be found in the Supplementary Material (Supporting Figure S1). The decay curves show similar results across different T_{RO}. However, the shortest T_{RO} of 1 ms shows an increased noise contribution in the measured signal. Figure 2b illustrates the noise influence in the lowest signal regime (30 mM). The left graph shows the duration of signal with a threshold at double the noise mean ($y \geq 2\,\mu_{noise}$). The right graph displays the corresponding number of echoes that were acquired within that time range. The results show that $T_{RO} \geq 2$ ms detects longer lasting signal above the noise threshold compared to T_{RO} of 1 ms. Furthermore, a sampling time of 2 ms permits acquisition of a high number of echo samples, particularly in faster decaying environments with higher agar concentrations. Based on these findings, the human in vivo measurements were acquired at an optimised T_{RO} of 2 ms.

Figure 3 depicts a series of echo reconstructions from phantom and in vivo measurements acquired at $T_{RO} = 2$ ms. The initial reconstructed image at TE_0 reveals the typically acquired

^{23}Na-density weighted image (53,54). The phantom reconstruction demonstrates that the signal intensities in the initial echo (TE_0, Figure 3a, top-left) reflect the ^{23}Na concentration, independent of the media, i.e. agar concentration. Subsequent echo images show the expected decrease in signal due to T2* relaxation, which reveal a dependency on the underlying structured media. In liquid, the ^{23}Na signal decays slower than ^{23}Na signal in the more solid solutions. Similar characteristics were observed in human in vivo measurements (Figure 3b), with longer lasting signal in fluid regions (CSF) compared to brain tissue.

Multi-Echo combination for image enhancement

Evidence that the signal decay curves show media- and tissue-specific characteristics is further seen in Figure 4b (in vivo) and Supporting Figure S2 (phantom). Measurements of SNR over tissue regions of interest in the human in vivo data (Figure 4c) underscore this fact; ^{23}Na signal in fluid environments preserves higher SNR for longer, whereas SNR decays quicker in more structured environments. Despite the fast signal decay in tissue, it was found that the measurements in 3-4 echoes demonstrated signal above noise level in human tissue (dashed line in Figure 4b). This finding was directly translated into an image enhancement technique via averaging (Figure 5a). Figure 5b shows measured SNR (mean and standard error) in segmented brain regions over the number of echoes used for averaging, across all subjects. For tissue, it was verified that 3-4 averages achieved the most significant SNR increase (Supporting Table S1 in Supplementary Material). As expected, further averaging only provides negligible SNR improvements, as the loss of signal at higher echoes penalizes averaging results. Due to slower signal decay of fluids, CSF showed a greater and longer lasting SNR enhancement.

Figure 6 compares reconstruction results for single T_{RO} with averaged reconstructions in phantom measurements. While image SNR increases with longer T_{RO}, SNR enhancement can be partly retrieved at lower T_{RO} through averaging. The line profiles show no discernible edge blurring (Supporting Figure S3). Due to media-dependent T2* decay, intensity values in averaged reconstructions depict a combination of ^{23}Na concentration and T2* effects.

Estimation of parameter maps

Phantom

The result of the Maximum Likelihood Estimator in phantom measurements is shown in Figure 7a. Mean estimates and corresponding standard deviations within each vial are plotted in Figure 7b. In the liquid and 1% agar vial the estimation results reveal a primarily mono-exponential decay. For more solid environments (3% and 6% agar) $T2^*_{short}$ components can be differentiated with shorter decay times at higher agar level. The liquid phantom reveals the longest $T2^*_{long}$ decay, the influence of agar shortens the long component with no obvious dependency on agar concentrations. While there is only little variance between estimates at higher ^{23}Na concentrations (≥70mM), low ^{23}Na signal fitting results detect generally lower parameter estimates.

In vivo

Figure 8a displays the estimated T2* decay parameter maps for all subjects. A histogram of estimated values in segmented brain regions is shown in Figure 8b; with mean and standard deviations provided in Table 1. Both parameter maps allow for a distinction between fluid (CSF) and tissue regions – no $T2^*_{short}$ decay component was detected in fluid compartments; $T2^*_{long}$ decay estimates were higher for fluid than tissue compartments. While differentiation between CSF and tissue was found, intra-tissue delineation between gray and white matter is indeterminable. Fitting results over a range of initial conditions was found to lead to insignificant variations in decay estimates (±0.5ms in $T2^*_{short}$, ±2ms in $T2^*_{long}$; data not shown).

The two-step estimation procedure described in Methods incorporated the detection of mono-exponential decay through a plausibility check on the $T2^*_{short}$ estimate. Figure 9 shows a binary mask of voxels that were fit as mono-exponential decay (i.e. fluid signal region) compared with the CSF segmentation based on the MP2RAGE ^{1}H-based acquisition across all subjects. It should be noted that the CSF maps are fractional maps that originate from interpolation of binary segmentation masks onto the coarser ^{23}Na resolution.

Discussion

3D-MERINA presents a time-efficient imaging approach that enables the estimation of multiple parameter maps from a single acquisition. The idea of filling vacant ^{23}Na acquisition time with additional imaging has been explored previously; SISTINA (43) as well as phase cycling and gradient selection difference imaging (44,55) describe methods for the simultaneous acquisition of multiple ^{23}Na images. Their focus lies on the detection of ^{23}Na-density weighted images, together with direct (SISTINA) or indirect (pc/gsDIM) detection of triple quantum coherences, in order to isolate the intra-cellular ^{23}Na signal. In contrast, our work presents an acquisition scheme that focuses on the signal decay characteristics, while also maintaining ^{23}Na-density image contrasts.

^{23}Na-MRI is most applicable to high-field MRI (≥ 7T) given the significant gain in signal strength. However, higher fields are more prone to SAR limitations often leading to longer TR. In ^{23}Na-density weighted acquisitions, a full relaxation of the longitudinal magnetization requires a prolonged TR. 3D-MERINA fills this vacant acquisition time through measuring additional signal echoes, and reveals more detailed information of macroscopic structures beyond ^{23}Na-density. 3D-MERINA can be used to infer ^{23}Na-density maps (estimated from the initial TE_0-image) as well as bi-exponential T2* maps (estimated from time-series of echoes) in one acquisition protocol. The additional maps come at no cost in scan time and SAR exposure since the imaging protocol times are dictated by ^{23}Na-density weighted conditions and all imaging is performed with single 90° RF-pulses. It should be noted that the total scan time of 26 minutes is based on the choice of TR and the number of measured projections. While TR is relatively fixed due to the full relaxation constraint, the number of projections remains at the operator's discretion. A low number of projections decreases scan time, however acquisitions well below the Nyquist sampling condition result in a degradation of image quality. It should be noted that studies with a much lower number of projections showed the possibility of achieving comparable results (53).

Given the time range of $T2^*_{short}$ decay in biological tissue, a fast sampling scheme is crucial for the characterization of signal decay. Investigations into the effect of T_{RO} on SNR and PSF in 3D radial ^{23}Na-acquisition suggested an optimal sampling time between ~2-4 ms in

biological tissue (7). The experimental results in this study confirm this finding; while a faster readout of 1 ms facilitates the detection of more echoes, the higher noise disturbances lead to a shortening of high SNR data points (Figure 2).
Our experiment was based on a fixed resolution and FOV and revealed the shortest optimal T_{RO} at 2 ms. While theoretical investigations based on point-source objects suggest an optimized T_{RO} solely based on expected T2 decay values, common scanning situations with larger objects are expected to show less SNR decrease (7,46). A reduction in k_{max}, i.e. projection length, will aid the detection of faster echoes at the cost of lower image resolution.

Signal averaging for image enhancement showed good SNR improvement in brain tissue when restricting the averaging to early echoes. Under the absence of relaxation-based signal loss, it is well known that signal averaging provides an increase in image SNR by a factor of $\sqrt{n}$ for n signal averages. Due to the slower relaxation decay, this theoretical SNR improvement is closest achieved in fluid signal regions. However, gray and white matter regions also show a clear improvement in SNR.

Given the relatively low SNR regime of ^{23}Na-MRI, gaining an SNR increase without additional SAR or measurement time is of great value. However, the concomitant increase of SNR in CSF areas may reduce the visual tissue signal gain. Fluid suppression techniques (41) preparing the signal acquisition with a 180° pulse for CSF signal attenuation facilitate a suppression of CSF signal in the measurement process and can help exploit the full potential of tissue SNR enhancement.

It should be noted that alongside hardware components and the imaged object, ^{23}Na-image SNR depends on a variety of factors: sampling efficiency, projection number and image resolution, reconstruction filter, and sampling duration. The final image quality ultimately provides a compromise between resolution and imaging time. While very short sampling times are required for the detection of bi-exponential signal decay, short T_{RO} comes at the cost of reduced image SNR. Echo averaging provides a method to re-gain SNR and achieve

comparable image quality as achieved at longer T_{RO} (Figure 6). Averaging, however, leads to image intensities composed of a combination of ^{23}Na concentration and T2* signal decay.

Averaging methods may generally be prone to motion artifacts. However, in a 3D-MERINA acquisition setup, motion effects are minimal as the individual echoes are only separated by T_{RO} (in this study 2 ms), a timeframe in which no discernible motion at the nominal image resolution is expected. Another concern in image averaging lies in the T2*-blurring, that affects later echoes. A blurring of edges was, however, not observed in this study (Supporting Figure S3) since the optimal SNR improvement was found to be 3-4 averages. With a T_{RO} of 2 ms the total acquisition time of 3-4 echoes is under 15 ms and, hence, below other ^{23}Na acquisition techniques like TPI (6,9) and 3D cones (8) commonly using longer sampling trajectories. Imaging in this study was performed with a standard radial sampling scheme. The application of density-adapted trajectories is anticipated to enhance general image SNR and PSF (7,53).

A primary strength of 3D-MERINA is that gradient re-focused echoes allow for the estimation of T2* decays. ^{23}Na-signal in tissue is known to show fast bi-exponential decay originating from electric field interactions of spins in macromolecular environments. Given the low gyromagnetic ratio of ^{23}Na, T2* is expected to be a close correlate for T2 values. The estimation was performed for short and long T2* decay components using a Maximum Likelihood approach accounting for underlying Rician noise distribution. The resulting parameter maps show good agreement with previously reported values (27,50,56-59). This study captured 38 echoes allowing for a very accurate analysis of underlying noise. The echo spacing was 4 ms. Previous studies on slow T2* decay estimation were based on a significantly lower number of recorded echoes – 2 echoes (57); 10 echoes (56) – and mostly higher echo spacing – 25 ms (57); 3.6 and 10ms (56). These studies were performed at lower image resolutions and, furthermore, required the acquisition of several averages to enhance SNR characteristics.

To our knowledge this is the first mapping of $T2^*_{short}$ components in the human brain. Brain tissue short decay components are reported to be of the order of 0.5-3 ms. The

$T2^*_{short}$ parameter were generally estimated in this time range. However, close to the sinuses, i.e. areas of stronger B_0 inhomogeneities, $T2^*_{short}$ estimates deviated from the expected range. This is not surprising, given that T2* in these areas is probably not a close correlate to actual T2 values.

While the $T2^*_{short}$ estimates generally range within expected values (1,58) care needs to be taken given the wide distribution of estimates. This is unavoidable, given the low number of measurement points in the very short TE range. More reliable $T2^*_{short}$ maps require faster T_{RO} to increase the number of data points in the $T2^*_{short}$ time range. An increase of gradient strength and subsequent reduction of T_{RO} was found to result in poor SNR (Figure 3). Nevertheless, a decrease in k_{max} would lead to a similar speed up in readout and decrease echo spacing – at the cost of image resolution. A partial readout as applied in (56) can lead to a similar acceleration while maintaining spatial resolution.

In agar-doped solutions, ^{23}Na ions bind to polysaccharide molecules causing slower motion and consequently bi-exponential signal decay (25). The estimated $T2^*_{short}$ parameter in phantom experiments are in general agreement with previously reported values; $T2^*_{long}$ estimates are slightly longer than observed previously (25,52). The variation in parameter estimates even for $T2^*_{long}$ results from susceptibility artifacts between vials affecting T2* measurements. The estimation process detects fluid and solid environments in the short component mapping, $T2^*_{long}$ values are higher in fluid environments and decrease in solid media. The effect of lower t_c is less pronounced in the $T2^*_{long}$ component (59) and, hence, does not show a clear differentiation between agar level.

Despite the agreement of fitting parameter with reported values, it should be noted that bi-exponential fitting is known to be an ill-posed problem with lower accuracy and precision at low SNR. Incorporating Rician noise distribution into the estimation process has, however, been shown to give the best performance (60).

The initial results in this work have focused on the general mapping of tissue signal decay characteristics. The maximum likelihood estimation process does not account for partial volume effects. Given the relatively coarse resolution in ^{23}Na imaging, a more complete

model could include a combination of bi- and mono-exponential decay with fractional volume components. The tri-exponential model is, however, more difficult to fit robustly.

The two-step estimation process allowed for an inference of fluid signal contributions. The fluid mono-exponential masks showed good agreement with CSF masks obtained from ^{1}H-acquisitions, demonstrating the potential to infer underlying macroscopic structures. The fitting procedure detected mono-exponential decay even in regions with low (<20%) CSF volume fractions, which suggests a strong sensitivity of the estimation algorithm towards fluid-signal influence.

Difference images for the suppression of fluid ^{23}Na signal were first proposed in 1989 (58). Recent studies of double-echo bi-exponentially weighted ^{23}Na-MRI (42,44,55) investigated the use of difference imaging approaches to achieve image contrast featuring cellular ^{23}Na component information as achieved through multi-quantum filtered techniques. The use of multi-echo decay data as demonstrated in this work enables detailed investigation of such contrast mechanisms.

Conclusion

This work presents 3D-MERINA, a time-efficient imaging approach for a single acquisition from which multiple parameter maps can be derived. The method will facilitate a detailed investigation of pathologies by enabling a comprehensive investigation of ^{23}Na MR-signal properties – from ^{23}Na-density to signal decay characteristics providing insight into slow (tissue) and fast (fluid) motion regimes.

Acknowledgements

We acknowledge the facilities, and the scientific and technical assistance of the Australian National Imaging Facility at the Melbourne Brain Centre Imaging Unit. The work was also supported by a research collaboration agreement with Siemens Healthcare. The MP2RAGE data was acquired with a prototype sequence provided by Siemens Healthcare.

Jon Cleary is funded by a University of Melbourne McKenzie fellowship. Brad Moffat is supported by the Australian National Imaging Facility (NIF).

List of Tables

Table 1: In vivo T2* fitting results across tissue compartments

T2* short [ms]			T2* long [ms]		
CSF	GM	WM	CSF	GM	WM
	2.02±1.67	1.99±2.09	57.2±6.6	25.9±8.3	22.4±7.8

Mean and standard deviation of estimated decay parameters in CSF, gray matter and white matter across all investigated subjects.

List of Figures

FIG 1: (a) Pulse sequence diagram for 3D-MERINA with definition of timing parameters. (b) Simplified 2D illustration of echo sampling. During each excitation several gradient re-focused echoes are acquired. First echo is measured as half-projection, subsequent echoes are sampled as full-projections along the same angle.

FIG 2: (a) Magnitude signal from the central voxel of 30 mM saline phantom vials at high agar concentration (6%) and in liquid media. Curves plot signal decay measured at T_{RO} ranging from 1-5 ms. T_{RO} of 1 ms (blue) shows stronger noise contribution. (b) Duration (left) and number of echoes (right) with signal above 2 μ_{noise} in 30 mM NaCl vials across measured T_{RO}.

FIG 3: Reconstruction of first 9 echoes of phantom (a) and in vivo (b) measurements (T_{RO} = 2 ms). Phantom composition is depicted on the left. The curved horizontal alignment resulted from the use of a head-shaped cushion for stabilization. The initial echo image (TE_0 = 0.4 ms) demonstrates the ^{23}Na-density weighted image; the signal-time-series of subsequent TE reconstructions reveal signal decay characteristics specific to the underlying media.

FIG 4: Signal evolution over echo reconstructions. TE_0 image of in vivo acquisition (a) indicating location of plotted voxel decay (b). The CSF voxel location has been carefully chosen in the right ventricle to minimize partial volume contamination. Signal decay in voxel in in vivo measurement (b) show slower signal decrease in liquid environments (CSF) compared to tissues. Black dashed line indicates 2 μ_{noise} threshold. (c) depicts mean and standard deviation of SNR measurements across all subjects in segmented tissue regions (CSF, gray matter, white matter). Longer lasting signal in liquid regions lead to higher SNR in CSF at later echoes compared to gray and white matter.

FIG 5: (a) Reconstruction of averaged signal over n foremost echoes in vivo. (b) SNR measurements in segmented tissue compartments over n averages. Curves show mean and standard deviation of SNR across all subjects. Averaging was performed on raw complex k-space data before re-gridding and image reconstruction. An SNR increase is achieved in all ROIs for early echo averages, later averaging results decrease in SNR due to low signal in later echoes based on relaxation. Better SNR increase is achieved in fluid regions due to lower relaxation-based signal decrease between echoes. Tissue compartments show most significant gain in SNR for 3-4 echo-averages.

FIG 6: SNR values within vials of reconstructed images from T_{RO} 2 = ms (with and without averaging) and T_{RO} = 6 ms. Averaging increases SNR; in fast decaying solutions longer T_{RO} achieve better SNR than averaging.

FIG 7: (a) T2* maps of short and long component in phantom vials. (b) Mean estimates and standard deviation plotted over agar-concentration; Colors indicate saline concentrations. $T2^*_{long}$ maps delineate liquid from agar-doped vials. $T2^*_{short}$ parameter estimation differentiate higher agar concentrations (≥ 3%).

FIG 8: (a) T2* maps of short and long components across all subjects. (b) Histogram of estimated parameter over segmented brain regions. T2* maps show structural information, distinguishing tissue and fluid ^{23}Na signal areas. $T2^*_{long}$ estimation results agree with previous studies (1,56-58). $T2^*_{short}$ parameter show spread estimates with increased values in sinus regions.

FIG 9: Comparison between mono-exponential fit mask of detected fluid ^{23}Na regions and CSF masks obtained from ^{1}H-MP2RAGE acquisitions. The estimation of fluid ^{23}Na shows good agreement with fluid CSF regions from ^{1}H acquisition.

Supplementary Material

Supporting FIG S1: Magnitude signal from the central voxel of each vial in phantom experiments. Diagram rows showing concentration, columns indicating media. Curves plot signal decay measured at T_{RO} ranging from 1-5 ms. T_{RO} of 1 ms (blue) shows stronger noise contribution.

Supporting FIG S2: Signal evolution over echo reconstructions in Phantom. (a) TE_0 image of phantom indicating locations of plotted voxel decays. (b) Decay curves – markers distinguish agar level; colors indicate saline concentration – show distinct decay characteristics, with faster decreasing signal in more solid media (cross, pentagon). Initial signal intensities depend on saline concentrations.

Supporting FIG S3: (a) Reconstructed images from T_{RO} 2 = ms (with and without averaging) and T_{RO} = 6 ms. (b) Normalized line profiles along lines indicated in (a). Profiles show strong overlap. No disturbances in edge characteristics are observable.

Supporting Table S1: Mean SNR values and standard error in segmented tissue compartments and overall brain tissue for n echo averages and percentage SNR increase compared with single TE_0 reconstruction.

References

1. Madelin G, Lee JS, Regatte RR, Jerschow A. Sodium MRI: methods and applications. Prog Nucl Magn Reson Spectrosc 2014;79:14-47.
2. Boada FE, LaVerde G, Jungreis C, Nemoto E, Tanase C, Hancu I. Loss of cell ion homeostasis and cell viability in the brain: what sodium MRI can tell us. Curr Top Dev Biol 2005;70:77-101.
3. Thulborn KR. Quantitative sodium MR imaging: A review of its evolving role in medicine. Neuroimage 2016. doi: DOI: 10.1016/j.neuroimage.2016.11.056

4. Hilal SK, Maudsley AA, Simon HE, Perman WH, Bonn J, Mawad ME, Silver AJ, Ganti SR, Sane P, Chien IC. In vivo NMR imaging of tissue sodium in the intact cat before and after acute cerebral stroke. AJNR Am J Neuroradiol 1983;4(3):245-249.
5. Ra JB, Hilal SK, Oh CH, Mun IK. In vivo magnetic resonance imaging of sodium in the human body. Magn Reson Med 1988;7(1):11-22.
6. Boada FE, Gillen JS, Shen GX, Chang SY, Thulborn KR. Fast three dimensional sodium imaging. Magn Reson Med 1997;37(5):706-715.
7. Nagel AM, Laun FB, Weber MA, Matthies C, Semmler W, Schad LR. Sodium MRI using a density-adapted 3D radial acquisition technique. Magn Reson Med 2009;62(6):1565-1573.
8. Riemer F, Solanky BS, Stehning C, Clemence M, Wheeler-Kingshott CA, Golay X. Sodium ((23)Na) ultra-short echo time imaging in the human brain using a 3D-Cones trajectory. MAGMA 2014;27(1):35-46.
9. Lu A, Atkinson IC, Claiborne TC, Damen FC, Thulborn KR. Quantitative sodium imaging with a flexible twisted projection pulse sequence. Magn Reson Med 2010;63(6):1583-1593.
10. Inglese M, Madelin G, Oesingmann N, Babb JS, Wu W, Stoeckel B, Herbert J, Johnson G. Brain tissue sodium concentration in multiple sclerosis: a sodium imaging study at 3 tesla. Brain 2010;133(Pt 3):847-857.
11. Maarouf A, Audoin B, Pariollaud F, Gherib S, Rico A, Soulier E, Confort-Gouny S, Guye M, Schad L, Pelletier J, Ranjeva JP, Zaaraoui W. Increased total sodium concentration in gray matter better explains cognition than atrophy in MS. Neurology 2017;88(3):289-295.
12. Wetterling F, Gallagher L, Macrae IM, Junge S, Fagan AJ. Regional and temporal variations in tissue sodium concentration during the acute stroke phase. Magn Reson Med 2012;67(3):740-749.
13. Tsang A, Stobbe RW, Asdaghi N, Hussain MS, Bhagat YA, Beaulieu C, Emery D, Butcher KS. Relationship between sodium intensity and perfusion deficits in acute ischemic stroke. J Magn Reson Imaging 2011;33(1):41-47.
14. Schepkin VD. Sodium MRI of glioma in animal models at ultrahigh magnetic fields. NMR Biomed 2016;29(2):175-186.
15. Nagel AM, Bock M, Hartmann C, Gerigk L, Neumann JO, Weber MA, Bendszus M, Radbruch A, Wick W, Schlemmer HP, Semmler W, Biller A. The potential of relaxation-weighted sodium magnetic resonance imaging as demonstrated on brain tumors. Invest Radiol 2011;46(9):539-547.
16. Ouwerkerk R, Bleich KB, Gillen JS, Pomper MG, Bottomley PA. Tissue sodium concentration in human brain tumors as measured with 23Na MR imaging. Radiology 2003;227(2):529-537.
17. Zbyn S, Mlynarik V, Juras V, Szomolanyi P, Trattnig S. Evaluation of cartilage repair and osteoarthritis with sodium MRI. NMR Biomed 2016;29(2):206-215.
18. Marik W, Nemec SF, Zbyn S, Zalaudek M, Ludvik B, Riegler G, Karner M, Trattnig S. Changes in Cartilage and Tendon Composition of Patients With Type I Diabetes Mellitus: Identification by Quantitative Sodium Magnetic Resonance Imaging at 7 T. Invest Radiol 2016;51(4):266-272.
19. Madelin G, Babb JS, Xia D, Chang G, Jerschow A, Regatte RR. Reproducibility and repeatability of quantitative sodium magnetic resonance imaging in vivo in articular cartilage at 3 T and 7 T. Magn Reson Med 2012;68(3):841-849.
20. Bangerter NK, Tarbox GJ, Taylor MD, Kaggie JD. Quantitative sodium magnetic resonance imaging of cartilage, muscle, and tendon. Quant Imaging Med Surg 2016;6(6):699-714.

1. Zollner FG, Konstandin S, Lommen J, Budjan J, Schoenberg SO, Schad LR, Haneder S. Quantitative sodium MRI of kidney. NMR Biomed 2016;29(2):197-205.
2. Madelin G, Regatte RR. Biomedical applications of sodium MRI in vivo. J Magn Reson Imaging 2013;38(3):511-529.
3. Van der Mareel JR. Thermal Relaxation and Coherence Dynamics of Spin 3/2. I. Static and Fluctuating quadrupolar Interactions in the Multipole Basis. Concepts in Magnetic Resonance Part A 2003;19(2):97-115.
4. Hubbard PS. Nonexponential Nuclear Magnetic Resonance by Quadrupole Interactions. The Journal of Chemical Physics 1970;53(3):985-987.
5. Andrasko J. Nonexponential Relaxation of 23Na+ in agarose gels. Journal of Magnetic Resonance 1974;16(3):502-504.
6. Jaccard G, Stephen Wimperis, and Geoffrey Bodenhausen. Multiple-Quantum NMR Spectroscopy of S=3/2 Spins in Isotropic Phase: A new probe for multiexponential relaxation. The Journal of Chemical Physics 1986;85(11):6282-6293.
7. Berendsen HJ, Edzes HT. The observation and general interpretation of sodium magnetic resonance in biological material. Ann N Y Acad Sci 1973;204:459-485.
8. Delort A-M, Genevieve Gaudet, and Evelyne Forano. The use of chemical shift reagents and 23 Na NMR to study sodium gradients in microorganisms. Environmental Microbiology Methods and Protocols. Volume 16, Methods in Biotechnology: Springer; 2004. p 389-405.
9. Hutchison RB, Huntley, J. J., Jin, H., & Shapiro, J. I. Suppression of sodium nuclear magnetic resonance double-quantum coherence by chemical shift and relaxation reagents. The Journal of Chemical Physics 1992;97(12):8934-8940.
0. Boada F, Laverde G, Jungreis C, Nemoto E, Tanase C. Triple/Single quantum filtered sodium MRI of acute brain ischemia. Conf Proc IEEE Eng Med Biol Soc 2005;1:731-734.
1. Fleysher L, Oesingmann N, Inglese M. B(0) inhomogeneity-insensitive triple-quantum-filtered sodium imaging using a 12-step phase-cycling scheme. NMR Biomed 2010;23(10):1191-1198.
2. Griffey RH, Griffey BV, Matwiyoff NA. Triple-quantum-coherence-filtered imaging of sodium ions in vivo at 4.7 tesla. Magn Reson Med 1990;13(2):305-313.
3. Mirkes C, Shajan G, Bause J, Buckenmaier K, Hoffmann J, Scheffler K. Triple-quantum-filtered sodium imaging at 9.4 Tesla. Magn Reson Med 2016;75(3):1278-1289.
4. Tsang A, Stobbe RW, Beaulieu C. Triple-quantum-filtered sodium imaging of the human brain at 4.7 T. Magn Reson Med 2012;67(6):1633-1643.
5. Wimperis S, and Brian Wood. Triple-Quantum Sodium Imaging. Journal of Magnetic Resonance 1991;95(2):428-436.
6. Chang G, Madelin G, Sherman OH, Strauss EJ, Xia D, Recht MP, Jerschow A, Regatte RR. Improved assessment of cartilage repair tissue using fluid-suppressed (23)Na inversion recovery MRI at 7 Tesla: preliminary results. Eur Radiol 2012;22(6):1341-1349.
7. Feldman RE, Stobbe R, Watts A, Beaulieu C. Sodium imaging of the human knee using soft inversion recovery fluid attenuation. J Magn Reson 2013;234:197-206.
8. Lee JS, Xia D, Madelin G, Regatte RR. Sodium inversion recovery MRI on the knee joint at 7 T with an optimal control pulse. J Magn Reson 2016;262:33-41.
9. Madelin G, Lee JS, Inati S, Jerschow A, Regatte RR. Sodium inversion recovery MRI of the knee joint in vivo at 7T. J Magn Reson 2010;207(1):42-52.
0. Nagel AM, Amarteifio E, Lehmann-Horn F, Jurkat-Rott K, Semmler W, Schad LR, Weber MA. 3 Tesla sodium inversion recovery magnetic resonance imaging allows for improved visualization of intracellular sodium content changes in muscular channelopathies. Invest Radiol 2011;46(12):759-766.
1. Stobbe R, Beaulieu C. In vivo sodium magnetic resonance imaging of the human brain using soft inversion recovery fluid attenuation. Magn Reson Med 2005;54(5):1305-1310.

2. Qian Y, Panigrahy A, Laymon CM, Lee VK, Drappatz J, Lieberman FS, Boada FE, Mountz JM. Short-T2 imaging for quantifying concentration of sodium (23 Na) of bi-exponential T2 relaxation. Magn Reson Med 2014;74:162-174.
3. Fiege DP, Romanzetti S, Mirkes CC, Brenner D, Shah NJ. Simultaneous single-quantum and triple-quantum-filtered MRI of 23Na (SISTINA). Magn Reson Med 2013;69(6):1691-1696.
4. Benkhedah N, Bachert P, Semmler W, Nagel AM. Three-dimensional biexponential weighted (23)Na imaging of the human brain with higher SNR and shorter acquisition time. Magn Reson Med 2013;70(3):754-765.
5. Saff EB, and Arno BJ Kuijlaars. Distributing many points on a sphere. The Mathematical Intelligencer 1997;19(1):5-11.
6. Rahmer J, Bornert P, Groen J, Bos C. Three-dimensional radial ultrashort echo-time imaging with T2 adapted sampling. Magn Reson Med 2006;55(5):1075-1082.
7. Nielles-Vallespin S, Weber MA, Bock M, Bongers A, Speier P, Combs SE, Wohrle J, Lehmann-Horn F, Essig M, Schad LR. 3D radial projection technique with ultrashort echo times for sodium MRI: clinical applications in human brain and skeletal muscle. Magn Reson Med 2007;57(1):74-81.
8. Gudbjartsson H, Patz S. The Rician distribution of noisy MRI data. Magn Reson Med 1995;34(6):910-914.
9. Smith SM, Jenkinson M, Woolrich MW, Beckmann CF, Behrens TE, Johansen-Berg H, Bannister PR, De Luca M, Drobnjak I, Flitney DE, Niazy RK, Saunders J, Vickers J, Zhang Y, De Stefano N, Brady JM, Matthews PM. Advances in functional and structural MR image analysis and implementation as FSL. Neuroimage 2004;23 Suppl 1:S208-219.
0. Perman WH, Turski PA, Houston LW, Glover GH, Hayes CE. Methodology of in vivo human sodium MR imaging at 1.5 T. Radiology 1986;160(3):811-820.
1. Shporer M, Civan MM. Effects of temperature and field strength on the NMR relaxation times of 23 Na in frog striated muscle. Biochim Biophys Acta 1974;354(2):291-304.
2. Boada FE, Christensen JD, Huang-Hellinger FR, Reese TG, Thulborn KR. Quantitative in vivo tissue sodium concentration maps: the effects of biexponential relaxation. Magn Reson Med 1994;32(2):219-223.
3. Romanzetti S, Mirkes CC, Fiege DP, Celik A, Felder J, Shah NJ. Mapping tissue sodium concentration in the human brain: a comparison of MR sequences at 9.4Tesla. Neuroimage 2014;96:44-53.
4. Thulborn K, Lui E, Guntin J, Jamil S, Sun Z, Claiborne TC, Atkinson IC. Quantitative sodium MRI of the human brain at 9.4 T provides assessment of tissue sodium concentration and cell volume fraction during normal aging. NMR Biomed 2016;29(2):137-143.
5. Benkhedah N, Bachert P, Nagel AM. Two-pulse biexponential-weighted 23Na imaging. J Magn Reson 2014;240:67-76.
6. Bartha R, Menon RS. Long component time constant of 23Na T*2 relaxation in healthy human brain. Magn Reson Med 2004;52(2):407-410.
7. Fleysher L, Oesingmann N, Stoeckel B, Grossman RI, Inglese M. Sodium long-component T(2)(*) mapping in human brain at 7 Tesla. Magn Reson Med 2009;62(5):1338-1341.
8. Ra JB, Hilal SK, Oh CH. An algorithm for MR imaging of the short T2 fraction of sodium using the FID signal. J Comput Assist Tomogr 1989;13(2):302-309.
9. Civan MM, and Mordechai Shporer. NMR of Sodium-23 and Potassium-39 in Biological Systems. Biological Magnetic Resonance. Volume 1: Springer; 1978. p 1-32.
0. Bouhrara M, Reiter DA, Celik H, Bonny JM, Lukas V, Fishbein KW, Spencer RG. Incorporation of Rician noise in the analysis of biexponential transverse relaxation in

cartilage using a multiple gradient echo sequence at 3 and 7 Tesla. Magn Reson Med 2015;73(1):352-366.

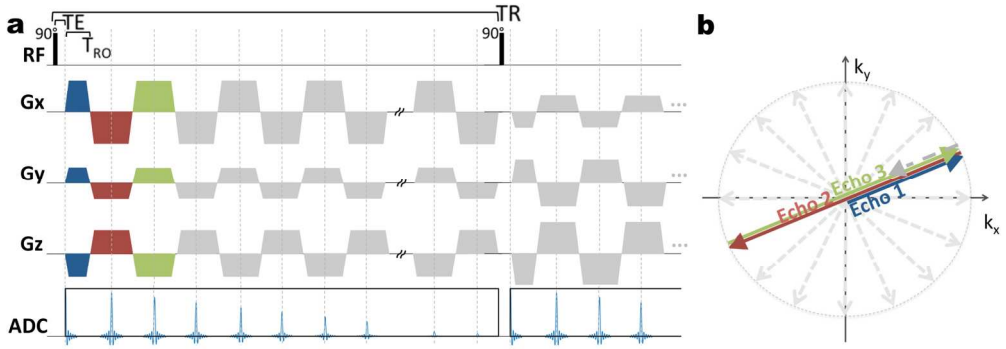

FIG 1: (a) Pulse sequence diagram for 3D-MERINA with definition of timing parameters. (b) Simplified 2D illustration of echo sampling. During each excitation several gradient re-focused echoes are acquired. First echo is measured as half-projection, subsequent echoes are sampled as full-projections along the same angle.

175x61mm (300 x 300 DPI)

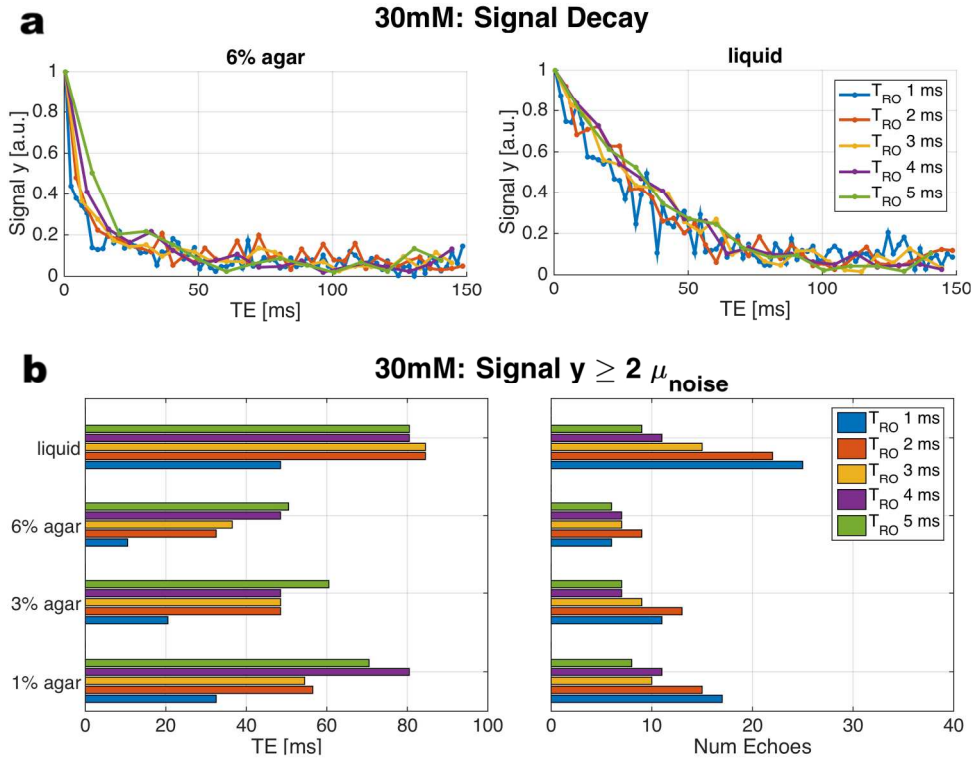

FIG 2: (a) Magnitude signal from the central voxel of 30 mM saline phantom vials at high agar concentration (6%) and in liquid media. Curves plot signal decay measured at TRO ranging from 1-5 ms. TRO of 1 ms (blue) shows stronger noise contribution. (b) Duration (left) and number of echoes (right) with signal above 2 μnoise in 30 mM NaCl vials across measured TRO.

180x137mm (300 x 300 DPI)

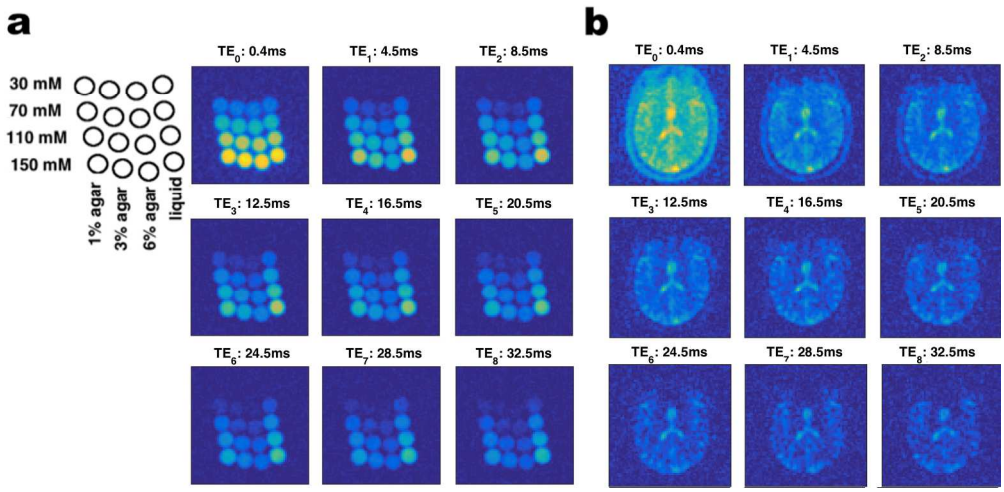

FIG 3: Reconstruction of first 9 echoes of phantom (a) and in vivo (b) measurements (TRO = 2 ms). Phantom composition is depicted on the left. The curved horizontal alignment resulted from the use of a head-shaped cushion for stabilization. The initial echo image (TE0 = 0.4 ms) demonstrates the 23Na-density weighted image; the signal-time-series of subsequent TE reconstructions reveal signal decay characteristics specific to the underlying media.

203x99mm (300 x 300 DPI)

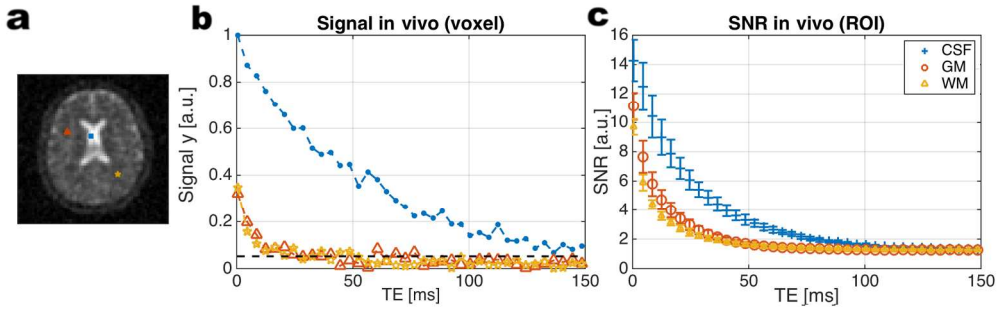

FIG 4: Signal evolution over echo reconstructions. TE0 image of in vivo acquisition (a) indicating location of plotted voxel decay (b). The CSF voxel location has been carefully chosen in the right ventricle to minimize partial volume contamination. Signal decay in voxel in in vivo measurement (b) show slower signal decrease in liquid environments (CSF) compared to tissues. Black dashed line indicates 2 μnoise threshold. (c) depicts mean and standard deviation of SNR measurements across all subjects in segmented tissue regions (CSF, gray matter, white matter). Longer lasting signal in liquid regions lead to higher SNR in CSF at later echoes compared to gray and white matter.

178x56mm (300 x 300 DPI)

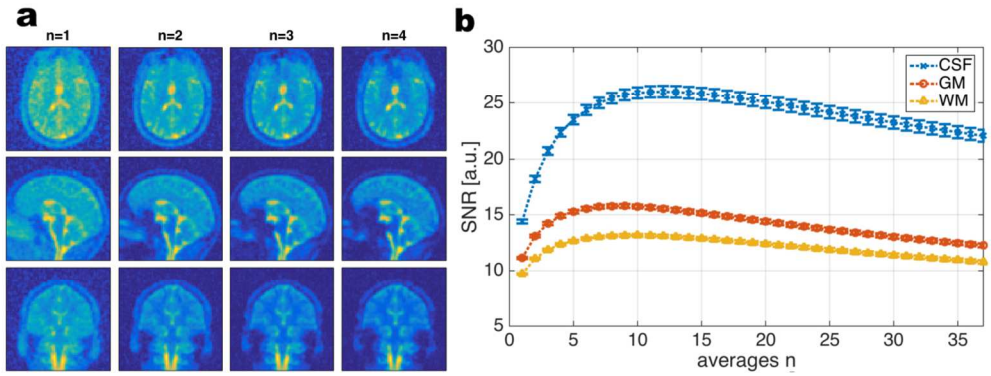

FIG 5: (a) Reconstruction of averaged signal over n foremost echoes in vivo. (b) SNR measurements in segmented tissue compartments over n averages. Curves show mean and standard deviation of SNR across all subjects. Averaging was performed on raw complex k-space data before re-gridding and image reconstruction. An SNR increase is achieved in all ROIs for early echo averages, later averaging results decrease in SNR due to low signal in later echoes based on relaxation. Better SNR increase is achieved in fluid regions due to lower relaxation-based signal decrease between echoes. Tissue compartments show most significant gain in SNR for 3-4 echo-averages.

115x42mm (300 x 300 DPI)

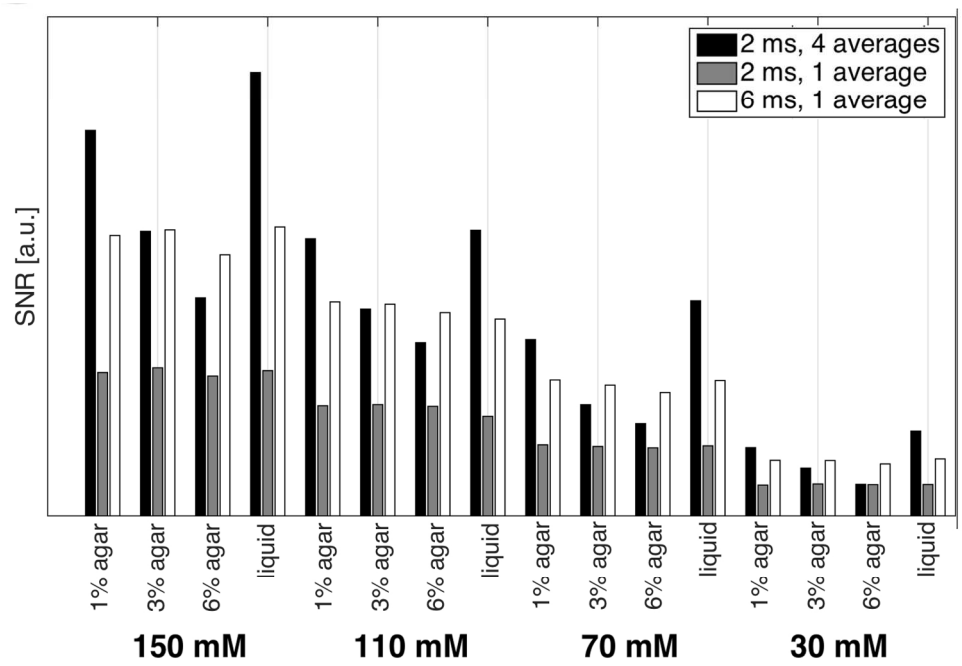

FIG 6: SNR values within vials of reconstructed images from TRO 2 = ms (with and without averaging) and TRO = 6 ms. Averaging increases SNR; in fast decaying solutions longer TRO achieve better SNR than averaging.

169x112mm (300 x 300 DPI)

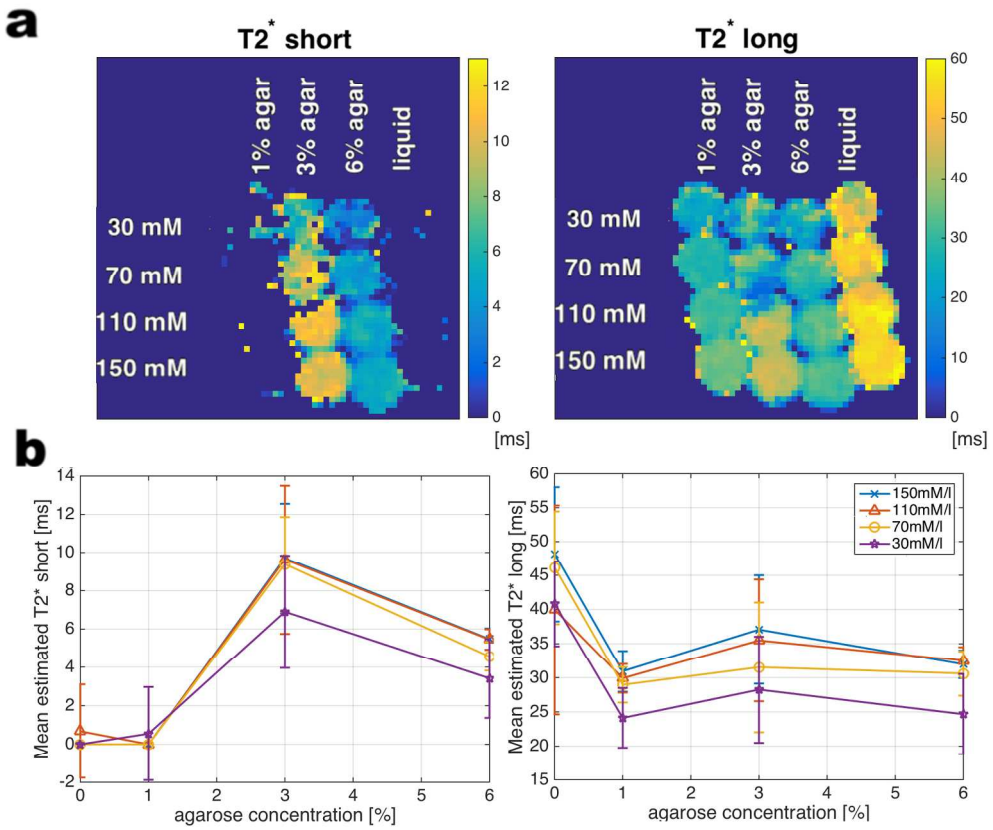

FIG 7: (a) T2* maps of short and long component in phantom vials. (b) Mean estimates and standard deviation plotted over agarose-concentration; Colors indicate saline concentrations. T2*long maps delineate liquid from agar-doped vials. T2*short parameter estimation differentiate higher agar concentrations (≥ 3%).

177x152mm (300 x 300 DPI)

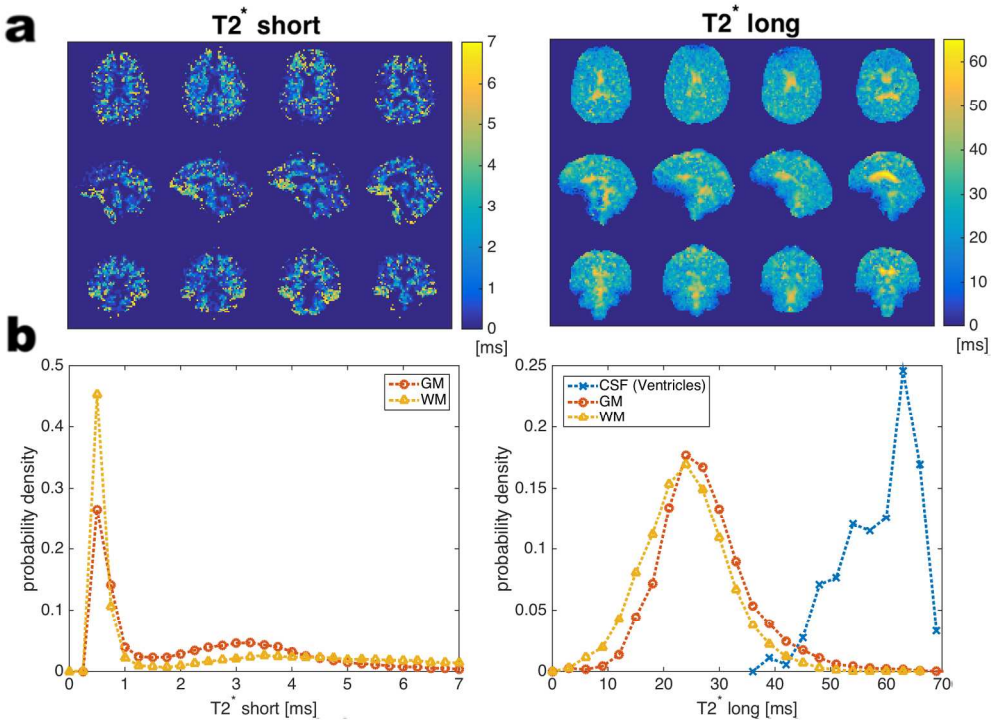

FIG 8: (a) T2* maps of short and long components across all subjects. (b) Histogram of estimated parameter over segmented brain regions. T2* maps show structural information, distinguishing tissue and fluid 23Na signal areas. T2*long estimation results agree with previous studies (1,56-58). T2*short parameter show spread estimates with increased values in sinus regions.

186x134mm (300 x 300 DPI)

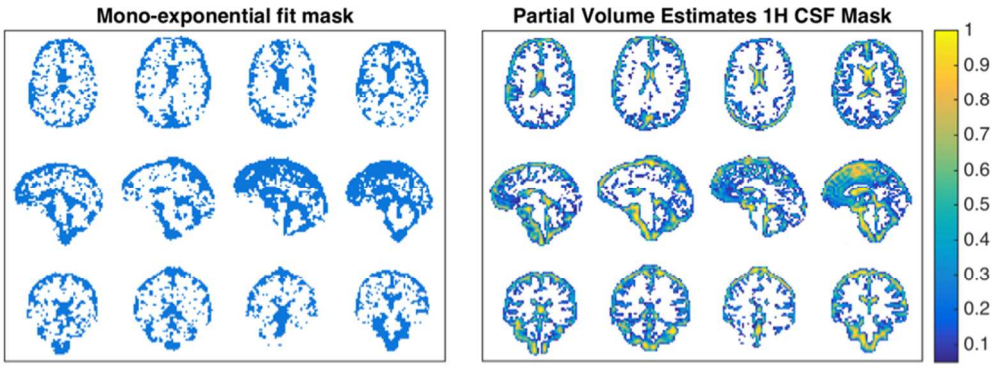

FIG 9: Comparison between mono-exponential fit mask of detected fluid 23Na regions and CSF masks obtained from 1H-MP2RAGE acquisitions. The estimation of fluid 23Na shows good agreement with fluid CSF regions from 1H acquisition.

76x27mm (300 x 300 DPI)

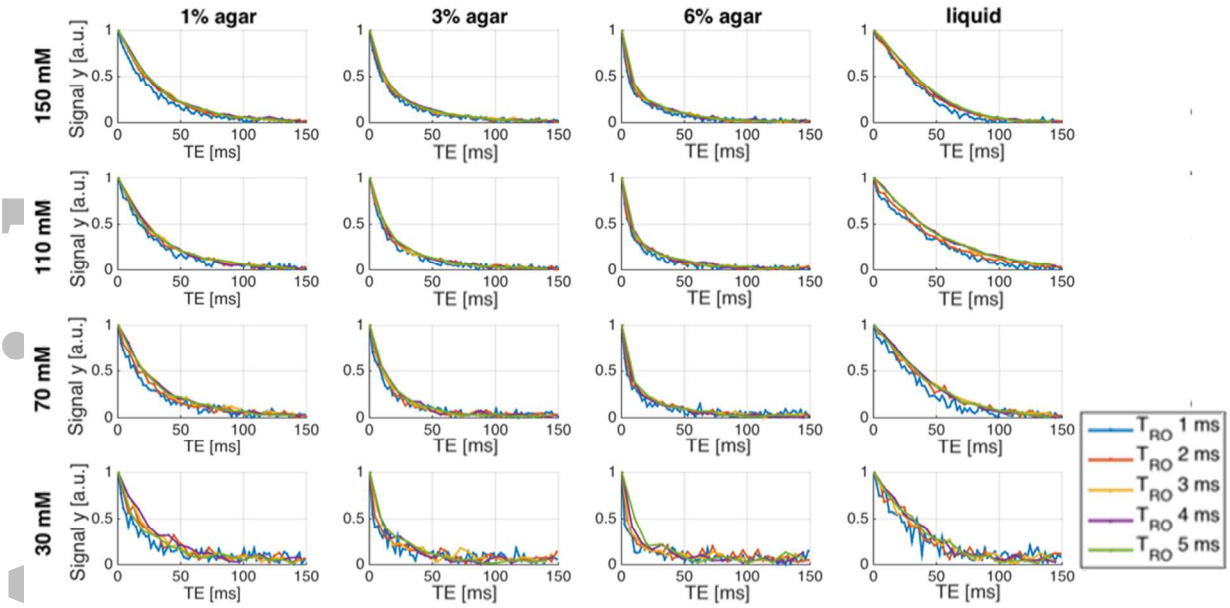

Supporting Figure S1: Magnitude signal from the central voxel of each vial in phantom experiments. Diagram rows showing concentration, columns indicating media. Curves plot signal decay measured at T_{RO} ranging from 1-5 ms. T_{RO} of 1 ms (blue) shows stronger noise contribution.

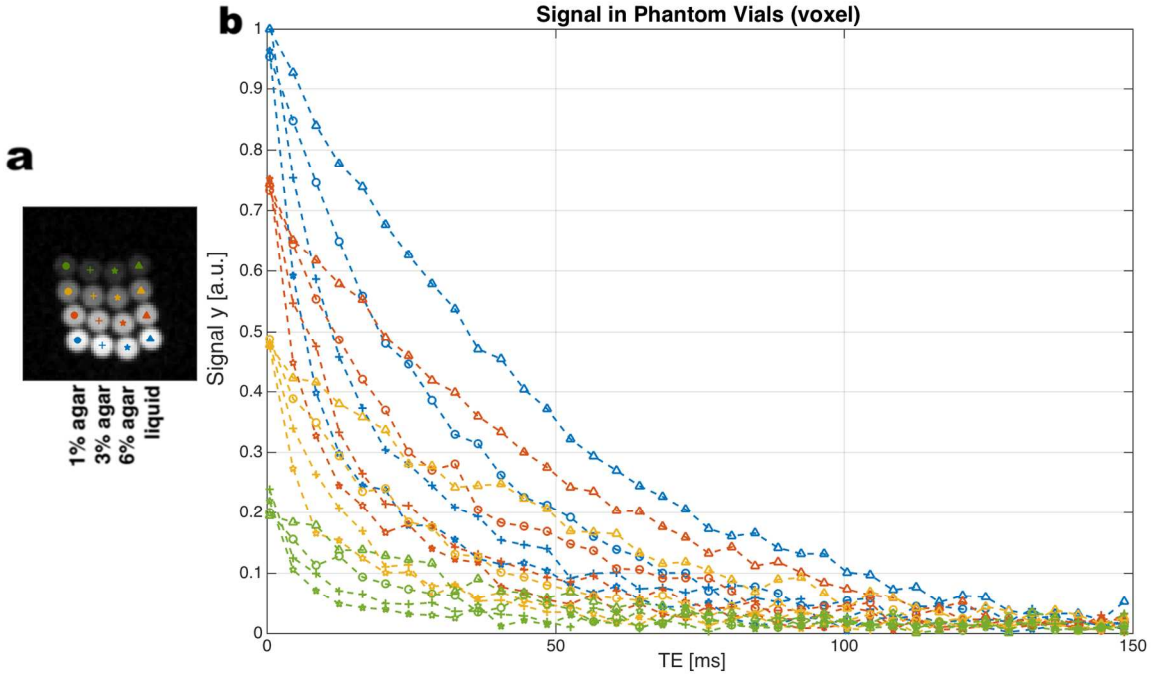

Supporting Figure S2: Signal evolution over echo reconstructions in Phantom. (a) TE_0 image of phantom indicating locations of plotted voxel decays. (b) Decay curves – markers distinguish agar level; colors indicate saline concentration – show distinct decay characteristics, with faster decreasing signal in more solid media (cross, pentagon). Initial signal intensities depend on saline concentrations.

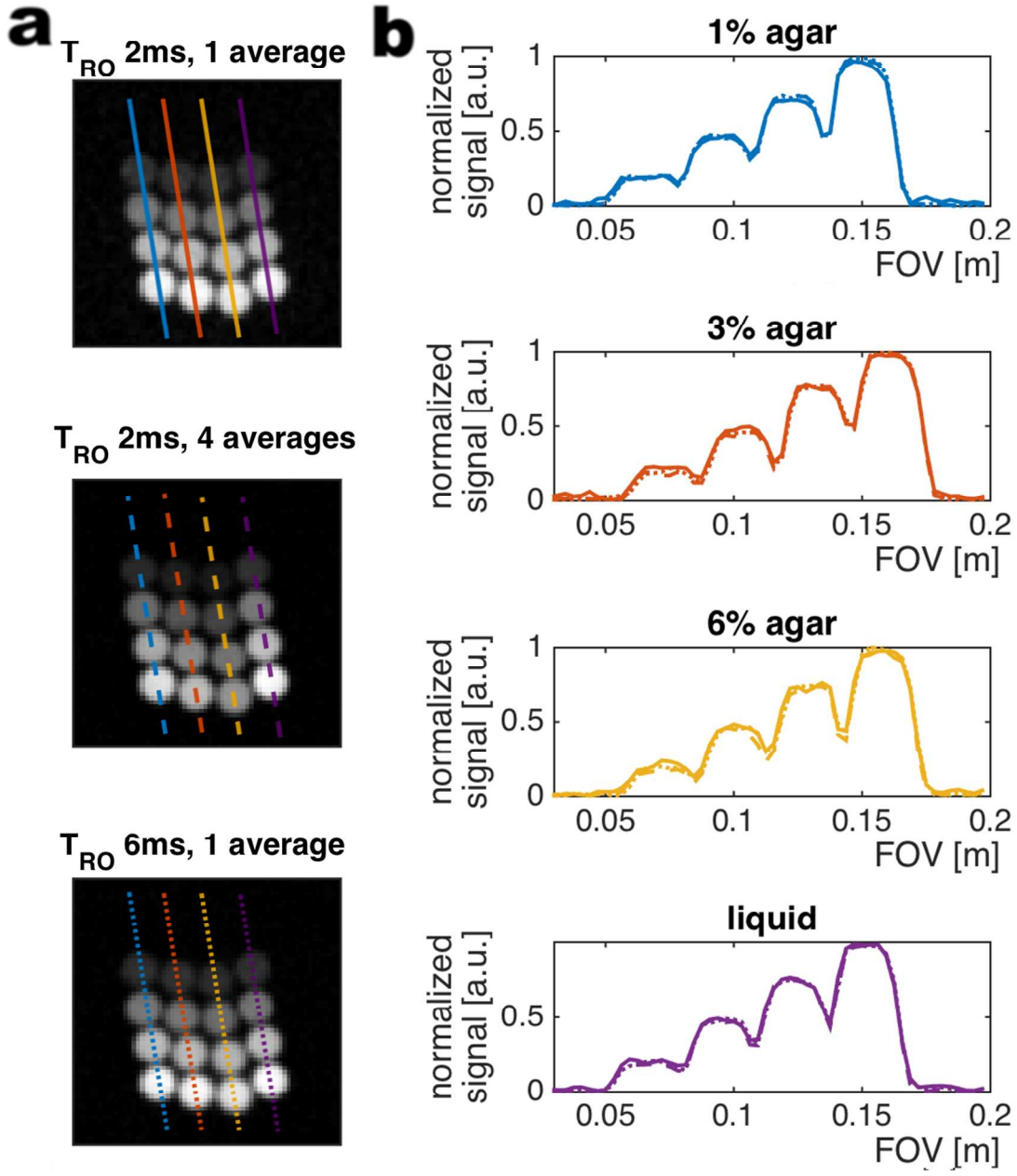

Supporting Figure S3: (a) Reconstructed images from T_{RO} 2 = ms (with and without

averaging) and T_{R0} = 6 ms. (b) Normalized line profiles along lines indicated in (a). Profiles show strong overlap. No disturbances in edge characteristics are observable.

Supporting Table S1: SNR in averaged in-vivo reconstructions across tissue compartments

	n = 1	n = 2	n = 3	n = 4	n = 5	n = 6	n = 7	n = 8	n = 9
CSF	14.4±0.18	18.3±0.28	20.7±0.38	22.4±0.38	23.5±0.41	24.4±0.44	25.0±0.46	25.4±0.48	25.7±0.5
Gain [%]	-	27.1	43.8	55.6	63.2	69.4	73.6	76.4	78.5
GM	11.1±0.09	13.1±0.12	14.2±0.14	14.9±0.15	15.3±0.16	15.5±0.17	15.7±0.17	15.8±0.17	15.8±0.18
Gain [%]	-	18.0	27.9	34.2	37.8	39.6	41.4	42.3	42.3
WM	9.7±0.05	11.1±0.08	11.9±0.09	12.4±0.1	12.7±0.11	12.9±0.12	13.0±0.12	13.1±0.12	13.2±0.13
Gain [%]	-	14.4	22.7	27.3	30.9	32.9	34.0	35.0	36.1
Brain tissue	10.5±0.07	12.2±0.1	13.2±0.12	14.1±0.13	14.3±0.13	14.5±0.14	14.6±0.15	14.6±0.15	14.6±0.15
Gain [%]	-	16.2	25.7	34.3	36.2	38.1	39.0	39.0	39.0

Mean SNR values and standard error in segmented tissue compartments and overall brain tissue for n echo averages and percentage SNR increase compared with single TE_0 reconstruction.

International Society for
Magnetic Resonance in Medicine

Young Investigator Awards Subcommittee
I.I. Rabi Award

THE UNIVERSITY OF MELBOURNE

12th April 2017

Re: Yasmin Blunck's Application for the 2018 Young Investigator Awards

To whom it may concern,

It is a pleasure to write a reference in support of this application for Yasmin who is a PhD student under my supervison.

Sodium MRI is an emerging method for studying brain physiology. There are exciting early indications that Sodium MRI may provide insights into neurological conditions where disordered sodium distribution likely plays a role. These conditions have great need for new diagnostic and prognostic biomarkers to guide treatment.

Yasmin is a 3rd year PhD student in my group. Yasmin's work focuses on the advancement of ^{23}Na-MRI at our 7T Siemens system. Her recent work aimed at a time-efficient acquisition approach together with an in-depth ^{23}Na signal analysis targeting at the inference of macroscopic ^{23}Na spin interactions. Her research offers great potential as an efficient measurement technique with the opportunity of gaining further insight into the ^{23}Na signal characteristics beyond ^{23}Na density.

Yasmin developed and implemented the new pulse sequence scheme independently and played a major part in the signal analysis. Furthermore, she provided a vital contribution to the preparation of this manuscript.

Yasmin has proven to be an outstanding student based on my 30 years of experience in supervising and teaching such people.

I am delighted to support Yasmin's application for the 2018 I.I. Rabi Young Investigator award and strongly believe that this honor would be a distinguished acknowledgement of her exciting research.

Yours sincerely,

R. J. Ordidge

Prof. Roger Ordidge

Prof. Roger Ordidge
Chair of Imaging Science
Director of Melbourne Brain Centre Imaging Unit
Department of Anatomy and Neuroscience
University of Melbourne Parkville Victoria 3010 Australia
Phone: +61 (0)3 8344 1953
Email: yblunck@student.unimelb.edu.au